Cation permeability and pore dynamics in TRPV1 ion channels.

Miriam García-Ávila[1], Javier Tello-Marmolejo[1,2], Tamara Rosenbaum[3] and León D. Islas[1*]

From:

[1]Department of Physiology, School of Medicine, UNAM, Mexico City, 04510, Mexico.

[2]Current affiliation: Department of Physics, University of Gothenburg, 405 30 Gothenburg, Sweden.

[3]Department of Cognitive Neuroscience, Instituto de Fisiología Celular, UNAM, Mexico City, 04510, Mexico.

*Correspondence to:

León D. Islas
Department of Physiology
School of Medicine
Universidad Nacional Autónoma de México (UNAM)
Circuito Escolar S/N, Ciudad Universitaria
Ciudad de México, 04510, México
leon.islas@gmail.com

ORCIDs

Javier Tello-Marmolejo: https://orcid.org/0000-0002-3665-793
L.D. Islas: https://orcid.org/0000-0002-7461-5214
Miriam García-Ávila: https://orcid.org/0000-0002-5326-7302
Tamara Rosenbaum: https://orcid.org/0000-0002-4791-3195

Abstract

The Transient Receptor Vanilloid 1 (TRPV1) is a non-selective ion channel, which is activated by several chemical ligands and heat. We have previously shown that activation of TRPV1 by different ligands result in single-channel openings with different conductance, suggesting that the selectivity filter is highly dynamic. TRPV1 is weakly voltage-dependent, here we sought to explore whether the permeation of different monovalent ions could influence the voltage-dependence of this ion channel. By using single-channel recordings, we show that TRPV1 channels undergo rapid

transitions to closed states that are directly connected to the open state, which may result from structural fluctuations of their selectivity filters. Moreover, we demonstrate that the rates of these transitions are ~~strongly~~ influenced by the permeant ion, suggesting that ion permeation regulates the voltage dependence of these channels.

Introduction

Transient receptor potential vanilloid (TRPV) channels are members of a superfamily of voltage-gated-like ion channels (Yu and Catterall, 2004). The first member of the TRPV family to be identified was TRPV1, which is a non-selective cationic channel involved in thermal sensation and which participates in the physiology of pain and inflammation (Rosenbaum et al., 2022). TRPV1 channels assemble as homotetramers, and each subunit contains large intracellular N-and C-terminal domains of complex architecture (Liao et al., 2013), and a transmembrane domain formed by six alpha helical membrane-spanning segments. Within this transmembrane domain, the transmembrane helices S1 to S4 form a helix bundle constituting a voltage sensor-like domain (VSLD), that does not seem to function as the voltage-sensor domains (VSD) present in canonical voltage-activated channels (Palovcak et al., 2015a), but which contains multiple binding sites for activating and regulatory molecules (Cao, 2020). The pore, which <u>encompasses</u> a selectivity filter and an activation gate, is formed by the S5 segment, a pore loop and a helix motif and the S6 segment (Liao et al., 2013).

TRPV1 can be activated by varied stimuli such as capsaicin, external pH < 5.4, heat, various ligands and voltage (Caterina and Julius, 2001; Jordt et al., 2000; Matta and Ahern, 2007; Grandl et al., 2010; Rosenbaum et al., 2022). Interactions with these stimuli lead to widening of the S6 activation gate, culminating in channel opening and ion permeation (Salazar et al., 2009). Importantly, these activating factors are allosterically coupled to the channel gate and also between them (Jara-Oseguera and Swartz, 2015).

64 Several structures of TRPV1 and related channels (TRPV1-4) have been solved by X-
65 ray crystallography and cryoEM methods (Liao et al., 2013; Zubcevic et al., 2018;
66 Shimada et al., 2020; Deng et al., 2018). These structures show that in the presence of
67 activators, the selectivity filter (SF) can adopt varying conformations, suggesting that
68 in these channels the SF is a highly dynamic structure (Zubcevic et al., 2018).
69 Functional experiments have shown that, while not an activation gate, the SF shows
70 dynamic accessibility changes (Jara-Oseguera et al., 2019). It has also been suggested
71 that voltage-induced conformational changes in this structure underlie the very small
72 voltage dependence of activation (Yang et al., 2020).

73 The dynamic character of the selectivity filter of TRPV1 has not been studied
74 functionally, although several lines of evidence point towards this characteristic. For
75 example, different agonists of TRPV1 can open the channel to distinct single-channel
76 conductance levels (Canul-Sánchez et al., 2018; Geron et al., 2018). Hence, we decided
77 to characterize the effect of the permeant ions on the gating of TRPV1. We observed
78 very rapid transitions to closed states that are directly connected to the open state
79 and that might represent structural fluctuations of the SF. The rates of these
80 transitions are strongly influenced by the permeant ion, in a manner that is consistent
81 with ion transport being involved in the regulation of gating of these channels.
82

83 **Methods**

84 *Cell culture and transfection.*

85 We used the HEK293 cell line from American Type Culture Collection (ATCC; RRID:
86 CVCL_0045) for heterologous expression of TRPV1. Cells were grown in Dulbecco´s
87 Modified Eagle Medium (DMEM, Invitrogen) with the addition of 10 % fetal bovine
88 serum (Invitrogen) and 1% of penicillin-streptomycin (Invitrogen) (referred to as
89 supplemented DMEM). Cultures were incubated at 37°C, in a 5 % CO_2 atmosphere.
90 Every 3 or 4 days, the cells were washed with PBS, followed by treatment with 1 ml of
91 0.05% trypsin-EDTA (Invitrogen) for 2 min, then 1 ml of supplemented DMEM was
92 added. Subsequently, the cells were mechanically dislodged and 80 µl of the cell
93 suspension were reseeded on 5 x 5 mm glass coverslips in 30 mm culture dishes with

94 2 ml of supplemented DMEM. After 1-2 days in culture, cells were cotransfected with
95 pcDNA3.1 plasmid with WT rat TRPV1 (rTRPV1) and pEGFP-N1 plasmid containing
96 the eGFP fluorescent protein using the jetPEI transfection reagent (Polyplus),
97 according to manufacturer's instructions. Single-channel recordings were done one
98 day after transfection, while macroscopic recordings were performed two or more
99 days after transfection.

100 *Electrophysiological recordings.*

101 The experiments were carried out in the inside-out configuration of the patch-clamp
102 recording technique (Hamill et al., 1981). Recordings were performed using a pipette
103 (extracellular) solution consisting of 130 mM NaCl, 10 mM HEPES and 5 mM EGTA, pH
104 7.4, and bath (intracellular) solutions with either 130 mM NaCl, KCl, RbCl, LiCl, NH_4Cl
105 or CsCl (depending on the experiment, as indicated in the figure legends), 10 mM
106 HEPES, and 5 mM EGTA, pH 7.4.

107 Currents were recorded with an EPC-10 patch-clamp amplifier (RRID:SCR_018399,
108 HEKA Elektronik) controlled by PatchMaster software (RRID:SCR_000034, HEKA
109 Elektronik). Borosilicate capillaries (Sutter instruments) were used to fabricate patch-
110 pipettes, which had a resistance after fire polishing of 4-6 MΩ for macroscopic
111 currents and 8-10 MΩ for single-channel recordings.

112 Macroscopic currents were filtered <u>with the build-in 4-pole Bessel filter of the EPC-10</u>
113 <u>at 1 kHz (-3dB) and sampled at 40 kHz while single-channel currents were filtered at</u>
114 <u>5 kHz and sampled at 50 kHz.</u>

115

116 *Analysis of macroscopic current recordings.*

117 The macroscopic conductance in each permeant ion condition was determined from
118 the current *I,* applying Ohm's law according to:

$$G = \frac{I}{V - V_{rev}}$$

119 where V is the test voltage and V_{rev} is the reversal potential. The conductance was
120 normalized to the maximum G_{max} and plotted as a function of voltage and was fit to a
121 Boltzmann function:

122 $$\frac{G}{Gmax} = \frac{1}{1+e^{\frac{z(V-V_{1/2})}{K_B T}}} \quad \text{Eq. 1}$$

123 where z is the apparent valence of gating in e_o, $V_{1/2}$ is the potential where G/G_{max}=0.5,
124 K_B is Boltzmann's constant and T the temperature in Kelvin (296 K). The apparent free
125 energy change of activation by voltage was estimated as $\Delta G_{ion} = zV_{1/2}$ from values
126 obtained for each ion from fits to Eq. 1. $\Delta\Delta G$ was estimated as ΔG_{ion}-ΔG_{Na}
127
128 *Analysis of single-channel recordings.*
129 Single-channel recordings were analyzed to determine the open probability, P_o.
130 Openings were detected employing the 50% threshold crossing method (Colquhoun
131 and Sigworth, 1995a). Single-channel traces were interpolated with a cubic spline
132 function before event detection. Dwell times (d_o) of open events and dwell times of
133 closed events (d_c) were compiled and used to determine P_o as:
134 $$P_o = \frac{d_o}{d_o+d_c} \quad \text{Eq. 2}$$
135 ~~The dwell times were also used to construct amplitude vs. open dwell time~~
136 ~~relationships.~~
137 Single-channel kinetics were analyzed by constructing open and closed dwell time
138 distributions using log-transformed histograms according to (Sigworth and Sine,
139 1987). Events shorter than the filter death time T_d were discarded. $T_d = 0.179/f_c$. At
140 f_c = 5 kHz, T_d = 36 μs. Bursts were defined as groups of openings separated by a closed
141 time longer than a critical time, t_c. This critical time was calculated from the closed
142 time distribution from recordings in Li^+, Na^+, Rb^+ and Cs^+ according to (Colquhoun and
143 Sakmann, 1985). Closed, open and burst length distributions were fit to a sum of
144 exponential components. The number of components and their parameters are given
145 in the figure legends.
146
147 *Analysis of fast single-channel current fluctuations.*
148 Fast current fluctuations are apparent in single-channel records both as increases in
149 the open-channel noise and as incomplete closing transitions. Since the half-amplitude
150 crossing method is not appropriate to study these extremely fast events, we chose to

151 analyze these fast kinetics by studying the all-points amplitude histograms compiled
152 from bursts of channel activity, employing an extension of the Beta-distribution
153 analysis developed by (Schroeder, 2015), which has been shown to be applicable to
154 systems with more than two states. This analysis relies on fitting of the all-points
155 amplitude histograms to theoretical distributions derived from time series of
156 simulated channel activity from specific kinetic models. These fits yield forward and
157 backward rate constants that were analyzed over varying conditions of permeant ion
158 and voltages. Bursts of channel openings were selected manually from recordings and
159 included short periods of no channel activity in order to adjust the zero current level.
160 Experimental all-points histograms were constructed by accumulating the currents
161 from these selected bursts.
162
163 *Model fitting.*
164 A simulated time series of channel openings and closings from specific Markov models
165 of gating was first generated employing a Monte Carlo method. For exponentially
166 distributed dwell times, any particular random duration of value d_i, in any closed or
167 open state, i, is calculated from rate constants as:
168 $$d_i = -\frac{1}{\sum_{i=1}^{j\neq i} k_{ij}} lnR_n \qquad \text{Eq. 3}$$
169 Here, k_{ij} are the rate constants leaving state i into state j and R_n is a uniformly
170 distributed random number from 0 to 1. Transition probabilities between sates i and j,
171 p_{ij} were calculated according to:
172 $$p_{ij} = \frac{k_{ij}}{\sum_{i=1}^{j\neq i} k_{ij}}$$
173 Once a time series is simulated, Gaussian noise with a variance similar to the variance
174 of the closed channel current level of each recording was added and the time series
175 was filtered by convolution with the impulse response of a Gaussian filter given by
176 (Colquhoun and Sigworth, 1995b):
177 $$H(t) = \frac{1}{\sqrt{2\pi}\sigma_g} exp\left(\frac{-t^2}{2\sigma_g^2}\right) \qquad \text{Eq. 4}$$
178 σ_g is related to the filter corner frequency f_c by:

$\sigma_g = \frac{\sqrt{(ln2)}}{2\pi f_c}$.

Simulated and filtered data are converted to an all-points amplitude histogram which is then fitted to the experimental histogram using a least-squares procedure and the fit parameters used to simulate a new time series until the fit error is minimized. We implemented a zero-order optimization algorithm with a number of iterations i = 100. The merit function was $R_n(i+1) < R_n(i)$, where $R_n(i)$ is an average of n least squares values between a simulation and the experimental data. The number of simulations per iteration, was n = 10. It was essential to average these least squares values $R_n(i)$ since the simulation is a random process and non-optimal values could produce a low R because of this randomness. Two types of steps were taken with equal probability in the variation of the fitting parameters. A small step that looks for the minimum R value and a large step. The large step was important to avoid getting stuck in local minima.

Experimental amplitude histograms were fitted to simulated histograms resulting from several models considering one open estate and one, two or more closed states with appropriate voltage dependent rate constants.

Fit to rate constants.

The voltage-dependence of each transition was calculated by plotting the rate constants as a function of voltage and fitting the data to the following function:

$$k = k(0) \cdot e^{\left(\frac{z\,V}{K_B T}\right)} \qquad \text{Eq. 5}$$

Here, $k(0)$ is the rate constant at 0 mV, z is the apparent charge associated with the transition, K_B is the Boltzmann constant, T is the temperature (296 K) and V is the voltage applied.

~~Fast transitions showed saturation at high voltages and were thus fitted using a subtraction of two exponential functions:~~

$$\cancel{k = k(0)_1 \cdot e^{\left(\frac{z_1 V}{K_B T}\right)} - k(0)_2 \cdot e^{\left(\frac{z_2 V}{K_B T}\right)}} \quad \cancel{\text{Eq. 6}}$$

Data were analyzed with Patchmaster (HEKA) and custom-written programs in Igor Pro 8 (RRID: SCR_000325, Wave-Metrics) and Python 3 using Jupyter Notebooks (RRID:SCR_008394).

208

209 *Statistical tests.*

210 Statistical comparisons were made by using one-way ANOVA with significance
211 determined from Tukey´s post hoc test. *$p < 0.05$ indicates statistical significance.

212

213 **Results**

214 In these experiments, we focused on outward currents carried by varying permeant
215 ions, in the nominal absence of divalent ions and presence of a constant extracellular
216 concentration of NaCl. These conditions were chosen since it has been shown that Ca^{2+}
217 can permeate, block and produce Ca^{2+}-calmodulin mediated desensitization of TRPV1
218 (Rosenbaum et al., 2004; Numazaki et al., 2003) and that extracellular Na^+ ions are
219 required for normal gating in TRPV1 (Jara-Oseguera et al., 2016).

220 ~~*Permeation and voltage dependence of TRPV1.*~~

221 Macroscopic currents through TRPV1 were activated by a saturating concentration of
222 capsaicin (CAP) of 10 μM and recorded in asymmetric ion concentrations, with Na^+
223 always present at 130 mM in the extracellular face of the channel. Outward currents
224 were carried by the test ion and were always preceded by recording of current in
225 symmetric Na^+ in the same patch, allowing the results to be compared over multiple
226 patches, taking as reference the condition in which the channel permeates Na^+ in both
227 directions. For example, red traces for only Na^+ vs. blue traces for Na^+/Li^+ (Figure 1A).
228 As can be seen from I-V curves normalized to the current in Na^+ at 130 mV, TRPV1
229 permeates monovalent ions (Figure 1B) (Caterina et al., 1997a).

230 Outward macroscopic currents are larger when the permeant ion has a larger ionic
231 radius like Cs^+ (1.6 $\dot{A}$). However, the reversal potential was not statistically different
232 from zero for each ion tested (Figure 1B), showing that the channel does not select
233 between monovalent ions. Conductance (G) vs. voltage (V) relationships, again,
234 normalized to G_{Na}, show that the magnitude of the maximal conductance at positive
235 voltages (G_{max}) depends on the permeant ion. These G-V curves were fitted to Eq. 1, to
236 estimate apparent charge, z and voltage of half activation $V_{1/2}$. Besides the effect on
237 G_{max}, the values of z and $V_{1/2}$, are different for each of the permeant ions studied;
238 specifically, there is a significant difference in the ΔΔG with Li^+ (Compared to Na^+,

239 Figure 1, D and E), which is brought about by a significant increase in z (increased
240 steepness of the G-V curve) and a negative shift of the $V_{1/2}$.
241 To understand why the macroscopic conductance is affected by the permeant ion, we
242 performed single-channel recordings in identical ionic conditions. Our single-channel
243 recordings in the inside-out configuration show a clear increase in the microscopic
244 conductance when larger ions permeate (Figure 2A). Since the reversal potential was
245 very close to zero for all ions (Figure 2B), to estimate the cation permeability, we used
246 the magnitude of the single-channel conductance, relative to the single-channel
247 conductance of Na^+ current in the same patch. We can estimate the permeability
248 sequence as: $Li^+ < Na^+ < K^+ < Rb^+ < NH_4^+ < Cs^+$ (Figure 2C).
249 Although the single-channel conductance explains in part the larger macroscopic
250 conductance when the permeant ion has a larger atomic radius, i.e., larger single-
251 channel conductance corresponds to larger macroscopic conductance, the microscopic
252 current-amplitudes observed by measuring single-channels (Figure 2B) do not fully
253 correspond to what is observed in macroscopic currents (Figure 1C). Specifically, the
254 single-channel conductance with Rb^+ is greater than in K^+, Na^+ and Li^+, unlike the
255 macroscopic results, where the conductance with Rb^+ is almost the lowest, only
256 comparable with the conductance with Li^+.
257 This difference suggests that when Rb^+ is the permeant ion at positive voltages, the
258 channel might gate differently. To test this possibility, we measured the single-
259 channel open probability according to Eq. 2, with different permeant ions. Figure 3A
260 shows that in the presence of Rb^+, the channel opens in short bursts, unlike the
261 openings in Na^+, which happen in long-lived bursts <u>at this concentration of capsaicin</u>.
262 Concurrently, the open probability is significantly smaller with Rb^+, while it is close to
263 the maximum <u>attained P_o at this capsaicin concentration (100 nM) and voltage in all</u>
264 <u>other ions tested (Figure 3B). Since the macroscopic current is proportional to the</u>
265 <u>product of P_o and single channel I-V,</u> this result reconciles the observed effects of ions
266 on microscopic and macroscopic conductance and reveals that the permeant ion
267 modulates gating of TRPV1. In particular, Rb^+ makes TRPV1 gate with lower open
268 probability.

269 To further explore the gating effects of permeant ions, we performed an analysis of
270 the kinetics of channel opening and closing. TRPV1 gating at the single-channel level is
271 complex (Hui et al., 2003), the open and closed dwell time histograms can be fitted by
272 a sum of three and four exponential components, respectively, indicating the presence
273 of multiple open and closed states (Supplementary figure 1 and Table I), with the
274 channel mostly opening in bursts. For comparison, we obtained the burst length
275 distributions in Li^+, Na^+, Cs^+ and Rb^+. As shown in Figure 4, burst length is also
276 multiexponential and the bursts become shorter when Rb^+ is the permeant ion. Burst
277 length distributions in Na^+, Li^+ and Cs^+ are very similar.
278 TRPV1 single-channel currents show a complex temporal structure, as mentioned
279 before. Moreover, the open state is rather unstable, showing many rapid closures or
280 flickers and an increased open channel noise. We observed that current flicker is more
281 noticeable with increasing ion size and voltage (Figure 2A), suggesting that this
282 flickery gating is a phenomenon that arises from the interaction of the permeant ion
283 with the pore of the channel.
284 Increased open channel noise can occur when channels undergo very rapid
285 transitions to closed states adjacent to the open state (Rauh et al., 2018). These
286 dynamics can be seen as excess noise in the power spectrum of the open channel
287 current or as a non-Gaussian distribution of the all-points current amplitude
288 histogram (Heinemann and Sigworth, 1991a). It has been shown that for a two-state
289 process, such as a unimolecular fast open channel block, the kinetics of the process
290 can be characterized from all-points current amplitude histograms by means of fitting
291 a beta distribution, which gives the amplitude of open events derived from a filtered
292 two-state stochastic process (Fitzhugh, 1983; Yellen, 1984).
293 When the fast process involves more than two states, there is no exact analytic
294 solution; however, it has been shown that the amplitude histograms can still be
295 compared with theoretical distributions derived from a simulation of an infinite
296 bandwidth process filtered with the same filter and frequency of experimental data. In
297 this way, different explicit Markov models can be used to extract rate constants from
298 extended beta distributions (Rauh et al., 2017; Schroeder, 2015). Importantly, this

299 approach is able to estimate kinetic events that are faster than the filter rise time
300 (Heinemann and Sigworth, 1991b).
301 Bursts of openings of TRPV1 contain both excess noise and apparently incomplete
302 closures (Figure 5A), these two phenomena make the amplitude histograms deviate
303 from a Gaussian distribution and give rise to "tails" of excess low amplitude events in
304 the all-points current amplitude histograms. Interestingly these tails become more
305 prominent when channels conduct larger ions.
306 Figure 5B compares histograms for all ions tested at 90 mV. It can be observed that
307 the smaller ions (Li^+ and Na^+) produce amplitude histograms that are roughly
308 Gaussian, while for the larger ions, the histograms deviate from Gaussian and are
309 asymmetric, with increased counts on the left arm of the histogram contributed by
310 amplitude values that approach the closed amplitude (Supplementary Figure 2). This
311 is made more evident in Figures 5C and D, which scale the histograms to the
312 maximum open amplitude for all ions and between the closed and open amplitudes,
313 respectively. These figures show greater excess noise for the openings with larger
314 cations.
315 To extract rate constants for the fast processes that give rise to these tails, we
316 employed extended beta distributions derived from the following Scheme I:

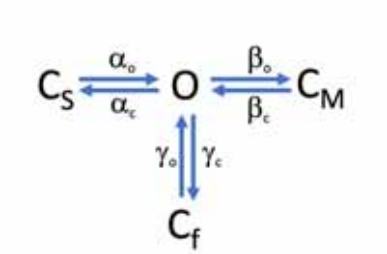

317

318 This scheme postulates the existence of three closed transitions adjacent to an open
319 state, each transition representing a slow, medium and fast equilibrium given by
320 alpha, beta and gamma rate constants, respectively. Although it is known that TRPV1
321 channels have many open and closed states, this simplified scheme can be applied to
322 the study of bursts of openings at sub saturating capsaicin concentrations, since the
323 effect of capsaicin is mainly to reduce the inter burst interval (Hui et al., 2003).

This scheme generates gating behavior that is very similar to the experimentally observed currents (Figure 5E) and the derived all-points histograms provide a good fit to the experimental histograms (Figure 5F). We also tested two simpler schemes with one open and one or two closed states and show that these cannot provide an adequate fit to the data (Supplementary figure 3; green and blue traces, respectively).

The voltage-dependence of the forward and backward rate constants obtained with the extended beta distribution method for all ionic conditions is shown in Figure 6. The slow opening transition (α_o) is determined mainly by longer lived closed states and shows a slight voltage-dependence in all ions, except ammonium, which tends to have a higher valence. Inversely, the closing transition (α_c) shows a higher voltage-dependence. Intermediate opening and closing transitions (β_o and β_c) have less voltage- dependence, while the fast transitions (γ_o and γ_c) are again more voltage dependent. The voltage-dependence of these transition rate constants was fit to a single exponential function of voltage (Eq. 5). ~~the fast-opening transitions show saturation at high positive voltages and can only be fitted with the subtraction of two exponential functions (Eq. 6),~~ (see Table II for all fitted parameter). An interesting finding derived from these measurements is that the rate constants for all three transitions are modulated by the permeant ion. When plotting the values of the rate constant at 0 mV (Figure 6B), the fast transition (γ_o) becomes faster for openings in the presence of larger ions, although the change is not very large. In contrast, the intermediate opening rate (β_o) clearly increase with the radius of the ion. The slow opening transition (α_o) shows a dependence on the ionic radius that is rather interesting, being fast for small and large ions and with a minimum for intermediate size ions. This slow transition mirrors the dependence of the open probability on the ionic radius (Figure 3B). ~~In general, rate constants, when compared at 0 mV, are faster with the larger ions such as Cs^+ and slower with smaller ions, although this is not a rule.~~

The ~~interplay between voltage and the effect of the permeant cation can be quantified by the~~ total charge associated with each of the three transitions is given by: $Z_i = (z_i^o - z_i^c)$, where the z_i's are the partial charges associated with each rate constant and

354 i = α, β, γ and o and c represent the opening or closing rate constant, respectively.
355 There is no difference between the values in the different permeant ion conditions
356 (Data not shown). ~~It is readily apparent that the smaller ions Li^+ and Na^+ are~~
357 ~~associated with a larger Z than say, Cs^+ or Rb^+.~~
358 ~~The finding that these transitions, which occur near the open state, are voltage~~
359 ~~dependent with a relatively high associated valence, that depends on the size of the~~
360 ~~ion suggest that the observed voltage-dependence of the macroscopic conductance~~
361 ~~might arise in part from the movement of ions in the pore's electric field. This is~~
362 ~~consistent with our previous observation that the macroscopic voltage-dependence at~~
363 ~~a saturating capsaicin concentration is modulated by the permeant ion (Figure 1D),~~
364 ~~with a tendency for smaller apparent charge for larger ions.~~ To compare the observed
365 voltage- dependence of rate constants with the macroscopic conductance, we
366 measured conductance at the same concentration of capsaicin at which rate constants
367 were estimated (100 nM) from single-channel recordings and contrasted it to the
368 prediction of Scheme I, using the measured rates and charges.
369 The open probability predicted by Scheme I is given by (derivation in Appendix):

370 $$P_O = \frac{K_s}{1+K_s+\frac{K_s}{K_m}+\frac{K_s}{K_f}} \qquad \text{Eq. 6}$$

371 With equilibrium constants K_i given by:

372 $$K_i = \frac{i_o(0)e^{\frac{q_{i_o}V}{KT}}}{i_c(0)e^{\frac{q_{i_c}V}{KT}}} \quad \text{, where } i = \alpha, \beta, \gamma \text{ and } \alpha=s,\ \beta=m,\ \gamma=f \qquad \text{Eq. 7}$$

373 Figures 7A and B depict macroscopic currents measured at saturating (10 μM) and
374 subsaturating (100 nM) capsaicin. Figure 7C shows G-V curves at 100 nM capsaicin for
375 all ions and Figure 7D shows the prediction of Scheme I (Eq. 6 and 7), using values
376 derived from measurements in Figure 6 (Table I). For all ions except ammonium, the
377 model shows good agreement with the data and suggest that the estimated apparent
378 charge associated with channel activation is modestly modulated by the permeant ion
379 (Figure 7E).
380
381 **Discussion**

382 TRPV1 is generally characterized as a cation permeable, non-selective channel with
383 slightly higher permeability to Ca^{2+} ions (Caterina et al., 1997b). Surprisingly, little is
384 known of the permeation mechanisms for cations in TRPV1. A study by (Samways and
385 Egan, 2011) showed single-channel recordings at a negative voltages that suggested
386 non-selective permeability of cations (also based in single-channel conductance) in
387 the order: Na^+ > Cs^+ > Li^+ > K^+. In this study, we have employed single-channel
388 recordings under bi-ionic conditions and measured a permeability sequence based on
389 the conductance at positive voltages, where the single-channel conductance is higher
390 and easier to measure. We observed a sequence Cs^+ > Rb^+ > K^+ > Na^+ > Li^+ for alkali
391 cations. Interestingly, this is identical with an Eisenman sequence of type I (Eisenman,
392 1962), which is produced by a weak field-strength cation binding site that favors
393 permeation of easily dehydrated larger ions. Molecular dynamics (MD) simulations
394 show that the TRPV1 pore may contain up to four binding sites for monovalent cation
395 permeation in which the free energy for Na^+ and K^+ is very similar (Jorgensen et al.,
396 2016), consistent with the almost identical permeability ratio for Na^+ and K^+.
397 However, no definitive permeation mechanism has been dilucidated for TRPV
398 channels.

399 Our data suggest that while non-selective, the pore of TRPV1 channels can regulate
400 the flux of monovalent cations based on the energetics of dehydration and can
401 differentiate between the size of ions, which is borne by the permeability sequence
402 obtained from single-channel records (Figure 2C).

403 MD simulations support a highly flexible selectivity filter in TRPV1 (Darré et al., 2015)
404 and our results indicated that gating can also be dynamic and is modulated by the
405 permeant ion. These results prompted us to explore the microscopic gating kinetics
406 and its possible dependence on the permeant ion. We observe that single-channel
407 kinetics are indeed modulated by the permeant ion, with Rb^+ reducing the burst
408 length and the open probability of the channels. The smaller ions Li^+ and Na^+ make it
409 more probable for the channel to open in long duration bursts and Cs^+ has an

410 intermediate effect. On top of these effects on closed and open dwell times, we
411 observed that the noise while the channel is open also varied with the permeant ion.

412 To study in detail this behavior, we employ the extended beta distribution method to
413 extract rate constants that arise from all closure events, including fast closures that
414 appear incomplete due to filtering, since simpler detection methods such as half-
415 amplitude threshold crossing are not appropriate to detect the contribution of rapid
416 incomplete closings.

417 In single-channel recording experiments, the intermediate transitions near the open
418 state seem to speed up when large ions permeate, leading to increased open channel
419 noise. This observation could be explained if small ions like Li^+ and Na^+ are able to
420 remain bound to the selectivity filter for longer times, due to their stronger
421 electrostatic electric field, and thus stabilize the open state, reducing fluctuations. In
422 contrast, the slow transitions are faster for small and big ions, with a minimum for
423 intermedia radii ions. This behavior is also observed in the burst length distributions
424 estimated from half-amplitude threshold crossing. Interestingly, the open probability
425 shows a similar behavior, with a minimum for Rb^+ ions. This is to be expected since
426 the slow transitions will contribute longer dwell times (in this case, longer closed
427 times) and have a larger contribution to the measured Po (Fig. 3).

428 The rapid fluctuations we observe are consistent with the existence of transitions
429 from the open state to closed states that are adjacent to the open state. It is likely that
430 these represent rapid pore dynamics derived from structural transitions. Cryo-EM
431 experiments have revealed that many TRPV channels, including TRPV1, can exist in
432 different pore conformations, even in the presence of activators (Zhang et al., 2021).
433 Functional data have also provided evidence that TRPV channels can adopt different
434 open conformations in the presence of different ligands (Benítez-Angeles et al., 2023;
435 Canul-Sánchez et al., 2018).

436 Experiments employing single-molecule FRET in Kir channels have directly shown
437 dynamic changes of the structure of the selectivity filter as a function of the presence

438 of Na^+ or K^+ ions (Wang et al., 2019). Related experiments employing solution nuclear
439 magnetic resonance have shown similar ion-dependent dynamics of the filter of a non-
440 selective ion channel, which has a filter structure more closely related to TRPV1's
441 (Lewis et al., 2021) and the intrinsic pore dynamics of TRPV1 has been demonstrated
442 directly by measuring the fluorescence of genetically encoded non-canonical amino
443 acids (Steinberg et al., 2017). It has also been demonstrated that the selectivity filter
444 can undergo conformational changes, although it is not a gate for small ions *per se*
445 (Jara-Oseguera et al., 2016).
446 An open question in TRPV channel biophysics, specially TRPV1, is the origin of the
447 mild voltage-dependence of the macroscopic conductance. As mentioned before, the
448 VLSD does not support a canonical function as a voltage sensor (Palovcak et al.,
449 2015b). It has recently been proposed that a conformational change that rearranges
450 the position of negatively charged residues at the extracellular entrance of the
451 selectivity filter is responsible for the voltage-dependence of TRPV1 gating, which is
452 equivalent to the displacement of ~0.55 elementary charges per channel (Yang et al.,
453 2020). We find that in the presence of saturating capsaicin, the apparent gating charge
454 depends on the identity of the permeant ion. The smallest alkali metal, Li^+, is
455 associated with a steeper G-V, with an apparent gating charge of 0.65 e_o as well as
456 activation at more negative voltages.

457 It is known that other types of ion channels obtain their voltage-dependence from the
458 concerted movements of permeant ions in the permeation pathway (Schewe et al.,
459 2016; Marchesi et al., 2012; Pusch et al., 1995) and that permeant blockers, also
460 moving in the pore's electric field, can produce highly voltage-dependent block
461 (Spassova and Lu, 1998). For example, in chloride ClC channels, voltage-dependence is
462 a result of the interaction of Cl^- ions with a protopore gate (Richard and Miller, 1990)
463 and in Kir channels, where permeating ions non-canonically regulate the voltage-
464 dependence of gating in these channels (Lu et al., 2001; Kurata et al., 2010). CNG
465 channels also display a small voltage-dependence at low open probabilities, although
466 its origin has not been clarified (Benndorf et al., 1999).

~~A fascinating observation derived from our study is that at relatively low concentration of capsaicin, were the open probability P_o ~0.4, the apparent gating charge is largest for the larger permeant cations, while at saturating concentration, with P_o = 0.98, the apparent gating charge is largest when the smaller ion (Li^+) permeates.~~

Acknowledgments

We thank Gisela Rangel, Manuel Hernández and Elsa Evaristo for excellent technical support. This work was supported by DGAPA-PAPIIT-UNAM grant No. IN215621 to L.D.I. and CONACyT (A1-S-8760) and DGAPA-PAPIIT-UNAM (IN200423) to T.R. M. G-A is a doctoral student from Programa de Doctorado en Ciencias Bioquímicas-UNAM and was supported by a doctoral thesis scholarship from CONACyT No. 776082.

References

Benítez-Angeles, M., A.E.L. Romero, I. Llorente, I. Hernández-Araiza, A. Vergara-Jaque, F.H. Real, Ó.E. Gutiérrez Castañeda, M. Arciniega, L.E. Morales-Buenrostro, F. Torres-Quiroz, R. García-Villegas, L.B. Tovar-Y-Romo, W.B. Liedtke, L.D. Islas, and T. Rosenbaum. 2023. Modes of action of lysophospholipids as endogenous activators of the TRPV4 ion channel. *J. Physiol.* 601:1655–1673. doi:10.1113/JP284262.

Benndorf, K., R. Koopmann, E. Eismann, and U.B. Kaupp. 1999. Gating by cyclic GMP and voltage in the alpha subunit of the cyclic GMP-gated channel from rod photoreceptors. *J Gen Physiol*. 114:477–90.

Canul-Sánchez, J.A., I. Hernández-Araiza, E. Hernández-García, I. Llorente, S.L. Morales-Lázaro, L.D. Islas, and T. Rosenbaum. 2018. Different agonists induce distinct single-channel conductance states in TRPV1 channels. *J. Gen. Physiol.* 150:1735–1746. doi:10.1085/jgp.201812141.

Cao, E. 2020. Structural mechanisms of transient receptor potential ion channels. *J. Gen. Physiol.* 152:e201811998. doi:10.1085/jgp.201811998.

Caterina, M.J., and D. Julius. 2001. The Vanilloid Receptor: A Molecular Gateway to the Pain Pathway. *Annu. Rev. Neurosci.* 24:487–517. doi:10.1146/annurev.neuro.24.1.487.

Caterina, M.J., M.A. Schumacher, M. Tominaga, T.A. Rosen, J.D. Levine, and D. Julius. 1997a. The capsaicin receptor: a heat-activated ion channel in the pain pathway. *Nature*. 389:816–824. doi:10.1038/39807.

501 Caterina, M.J., M.A. Schumacher, M. Tominaga, T.A. Rosen, J.D. Levine, and D. Julius. 1997b. The
502 capsaicin receptor: a heat-activated ion channel in the pain pathway. *Nature*. 389:816–
503 824. doi:10.1038/39807.

504 Colquhoun, D., and B. Sakmann. 1985. Fast events in single-channel currents activated by
505 acetylcholine and its analogues at the frog muscle end-plate. *J. Physiol.* 369:501–557.
506 doi:10.1113/jphysiol.1985.sp015912.

507 Colquhoun, D., and F.J. Sigworth. 1995a. Fitting and Statistical Analysis of Single-Channel Records.
508 *In* Single-Channel Recording. B. Sakmann and E. Neher, editors. Springer US, Boston, MA.
509 483–587.

510 Colquhoun, D., and F.J. Sigworth. 1995b. Fitting and Statistical Analysis of Single-Channel Records.
511 *In* Single-Channel Recording. B. Sakmann and E. Neher, editors. Springer US, Boston, MA.
512 483–587.

513 Darré, L., S. Furini, and C. Domene. 2015. Permeation and dynamics of an open-activated TRPV1
514 channel. *J. Mol. Biol.* 427:537–549.

515 Deng, Z., N. Paknejad, G. Maksaev, M. Sala-Rabanal, C.G. Nichols, R.K. Hite, and P. Yuan. 2018.
516 Cryo-EM and X-ray structures of TRPV4 reveal insight into ion permeation and gating
517 mechanisms. *Nat. Struct. Mol. Biol.* 25:252–260. doi:10.1038/s41594-018-0037-5.

518 Eisenman, G. 1962. Cation selective glass electrodes and their mode of operation. *Biophys. J.*
519 2:259–323. doi:10.1016/s0006-3495(62)86959-8.

520 Fitzhugh, R. 1983. Statistical properties of the asymmetric random telegraph signal, with
521 applications to single-channel analysis. *Math. Biosci.* 64:75–89. doi:10.1016/0025-
522 5564(83)90028-7.

523 Geron, M., R. Kumar, W. Zhou, J.D. Faraldo-Gómez, V. Vásquez, and A. Priel. 2018. TRPV1 pore
524 turret dictates distinct DkTx and capsaicin gating. *Proc. Natl. Acad. Sci.* 115.
525 doi:10.1073/pnas.1809662115.

526 Grandl, J., S.E. Kim, V. Uzzell, B. Bursulaya, M. Petrus, M. Bandell, and A. Patapoutian. 2010.
527 Temperature-induced opening of TRPV1 ion channel is stabilized by the pore domain. *Nat.*
528 *Neurosci.* 13:708–714.

529 Hamill, O.P., A. Marty, E. Neher, B. Sakmann, and F.J. Sigworth. 1981. Improved patch-clamp
530 techniques for high-resolution current recording from cells and cell-free membrane
531 patches. *Pflugers Arch*. 391:85–100.

532 Heinemann, S.H., and F.J. Sigworth. 1991a. Open channel noise. VI. Analysis of amplitude
533 histograms to determine rapid kinetic parameters. *Biophys. J.* 60:577–587.
534 doi:10.1016/S0006-3495(91)82087-2.

535 Heinemann, S.H., and F.J. Sigworth. 1991b. Open channel noise. VI. Analysis of amplitude
536 histograms to determine rapid kinetic parameters. *Biophys. J.* 60:577–587.
537 doi:10.1016/S0006-3495(91)82087-2.

538 Hui, K., B. Liu, and F. Qin. 2003. Capsaicin activation of the pain receptor, VR1: multiple open
539 states from both partial and full binding. *Biophys. J.* 84:2957–2968. doi:10.1016/S0006-
540 3495(03)70022-8.

541 Jara-Oseguera, A., C. Bae, and K.J. Swartz. 2016. An external sodium ion binding site controls
542 allosteric gating in TRPV1 channels. *eLife*. 5:e13356. doi:10.7554/eLife.13356.

543 Jara-Oseguera, A., K.E. Huffer, and K.J. Swartz. 2019. The ion selectivity filter is not an activation
544 gate in TRPV1-3 channels. *Elife*. 8:e51212.

545 Jara-Oseguera, A., and K.J. Swartz. 2015. Unraveling Allosteric Coupling Mechanisms in the TRPV1
546 Channel. *Biophys. J.* 108:124a. doi:10.1016/j.bpj.2014.11.695.

547 Jordt, S.-E., M. Tominaga, and D. Julius. 2000. Acid potentiation of the capsaicin receptor
548 determined by a key extracellular site. *Proc. Natl. Acad. Sci.* 97:8134–8139.
549 doi:10.1073/pnas.100129497.

550 Jorgensen, C., S. Furini, and C. Domene. 2016. Energetics of Ion Permeation in an Open-Activated
551 TRPV1 Channel. *Biophys. J.* 111:1214–1222. doi:10.1016/j.bpj.2016.08.009.

552 Kurata, H.T., M. Rapedius, M.J. Kleinman, T. Baukrowitz, and C.G. Nichols. 2010. Voltage-
553 dependent gating in a "voltage sensor-less" ion channel. *PLoS Biol.* 8:e1000315.
554 doi:10.1371/journal.pbio.1000315.

555 Lewis, A., V. Kurauskas, M. Tonelli, and K. Henzler-Wildman. 2021. Ion-dependent structure,
556 dynamics, and allosteric coupling in a non-selective cation channel. *Nat. Commun.*
557 12:6225. doi:10.1038/s41467-021-26538-8.

558 Liao, M., E. Cao, D. Julius, and Y. Cheng. 2013. Structure of the TRPV1 ion channel determined by
559 electron cryo-microscopy. *Nature*. 504:107–112. doi:10.1038/nature12822.

560 Lu, T., L. Wu, J. Xiao, and J. Yang. 2001. Permeant ion-dependent changes in gating of Kir2.1
561 inward rectifier potassium channels. *J. Gen. Physiol.* 118:509–522.
562 doi:10.1085/jgp.118.5.509.

563 Marchesi, A., M. Mazzolini, and V. Torre. 2012. Gating of cyclic nucleotide-gated channels is
564 voltage dependent. *Nat. Commun.* 3:973. doi:10.1038/ncomms1972.

565 Matta, J.A., and G.P. Ahern. 2007. Voltage is a partial activator of rat thermosensitive TRP
566 channels: Voltage-independent gating of TRPV1 and TRPM8. *J. Physiol.* 585:469–482.
567 doi:10.1113/jphysiol.2007.144287.

568 Numazaki, M., T. Tominaga, K. Takeuchi, N. Murayama, H. Toyooka, and M. Tominaga. 2003.
569 Structural determinant of TRPV1 desensitization interacts with calmodulin. *Proc. Natl.*
570 *Acad. Sci. U. S. A.* 100:8002–8006. doi:10.1073/pnas.1337252100.

571 Palovcak, E., L. Delemotte, M.L. Klein, and V. Carnevale. 2015a. Comparative sequence analysis
572 suggests a conserved gating mechanism for TRP channels. *J. Gen. Physiol.* 146:37–50.

573 Palovcak, E., L. Delemotte, M.L. Klein, and V. Carnevale. 2015b. Comparative sequence analysis
574 suggests a conserved gating mechanism for TRP channels. *J. Gen. Physiol.* 146:37–50.

575 Pusch, M., U. Ludewig, A. Rehfeldt, and T.J. Jentsch. 1995. Gating of the voltage-dependent
576 chloride channel CIC-0 by the permeant anion. *Nature*. 373:527–531.
577 doi:10.1038/373527a0.

578 Rauh, O., U.-P. Hansen, S. Mach, A.J.W. Hartel, K.L. Shepard, G. Thiel, and I. Schroeder. 2017.
579 Extended beta distributions open the access to fast gating in bilayer experiments-assigning
580 the voltage-dependent gating to the selectivity filter. *FEBS Lett.* 591:3850–3860.
581 doi:10.1002/1873-3468.12898.

582 Rauh, O., U.P. Hansen, D.D. Scheub, G. Thiel, and I. Schroeder. 2018. Site-specific ion occupation in
583 the selectivity filter causes voltage-dependent gating in a viral K+ channel. *Sci. Rep.*
584 8:10406. doi:10.1038/s41598-018-28751-w.

585 Richard, E.A., and C. Miller. 1990. Steady-state coupling of ion-channel conformations to a
586 transmembrane ion gradient. *Science*. 247:1208–1210. doi:10.1126/science.2156338.

587 Rosenbaum, T., A. Gordon-Shaag, M. Munari, and S.E. Gordon. 2004. Ca2+/Calmodulin Modulates
588 TRPV1 Activation by Capsaicin. *J. Gen. Physiol.* 123:53–62. doi:10.1085/jgp.200308906.

589 Rosenbaum, T., S.L. Morales-Lázaro, and L.D. Islas. 2022. TRP channels: a journey towards a
590 molecular understanding of pain. *Nat. Rev. Neurosci.* 23:596–610. doi:10.1038/s41583-
591 022-00611-7.

592 Salazar, H., A. Jara-Oseguera, E. Hernandez-Garcia, I. Llorente, I.I. Arias-Olguin, M. Soriano-Garcia,
593 L.D. Islas, and T. Rosenbaum. 2009. Structural determinants of gating in the TRPV1
594 channel. *Nat. Struct. Mol. Biol.* 16:704–710.

595 Samways, D.S.K., and T.M. Egan. 2011. Calcium-dependent decrease in the single-channel
596 conductance of TRPV1. *Pflüg. Arch. - Eur. J. Physiol.* 462:681–691. doi:10.1007/s00424-
597 011-1013-7.

598 Schewe, M., E. Nematian-Ardestani, H. Sun, M. Musinszki, S. Cordeiro, G. Bucci, B.L. de Groot, S.J.
599 Tucker, M. Rapedius, and T. Baukrowitz. 2016. A Non-canonical Voltage-Sensing
600 Mechanism Controls Gating in K2P K+ Channels. *Cell*. 164:937–949.
601 doi:10.1016/j.cell.2016.02.002.

602 Schroeder, I. 2015. How to resolve microsecond current fluctuations in single ion channels: The
603 power of beta distributions. *Channels*. 9:262–280. doi:10.1080/19336950.2015.1083660.

604 Shimada, H., T. Kusakizako, T.H. Dung Nguyen, T. Nishizawa, T. Hino, M. Tominaga, and O. Nureki.
605 2020. The structure of lipid nanodisc-reconstituted TRPV3 reveals the gating mechanism.
606 *Nat. Struct. Mol. Biol.* 27:645–652. doi:10.1038/s41594-020-0439-z.

607 Sigworth, F.J., and S.M. Sine. 1987. Data transformations for improved display and fitting of single-
608 channel dwell time histograms. *Biophys. J.* 52:1047–1054. doi:10.1016/S0006-
609 3495(87)83298-8.

610 Spassova, M., and Z. Lu. 1998. Coupled Ion Movement Underlies Rectification in an Inward-
611 Rectifier K+ Channel. *J. Gen. Physiol.* 112:211–221. doi:10.1085/jgp.112.2.211.

612 Steinberg, X., M.A. Kasimova, D. Cabezas-Bratesco, J.D. Galpin, E. Ladron-de-Guevara, F. Villa, V.
613 Carnevale, L. Islas, C.A. Ahern, and S.E. Brauchi. 2017. Conformational dynamics in TRPV1
614 channels reported by an encoded coumarin amino acid. *eLife*. 6:e28626.
615 doi:10.7554/eLife.28626.

616 Wang, S., S.-J. Lee, G. Maksaev, X. Fang, C. Zuo, and C.G. Nichols. 2019. Potassium channel
617 selectivity filter dynamics revealed by single-molecule FRET. *Nat. Chem. Biol.* 15:377–383.
618 doi:10.1038/s41589-019-0240-7.

619 Yang, F., L. Xu, B.H. Lee, X. Xiao, V. Yarov-Yarovoy, and J. Zheng. 2020. An Unorthodox Mechanism
620 Underlying Voltage Sensitivity of TRPV1 Ion Channel. *Adv. Sci.* 7:2000575.
621 doi:10.1002/advs.202000575.

622 Yellen, G. 1984. Ionic permeation and blockade in Ca2+-activated K+ channels of bovine
623 chromaffin cells. *J. Gen. Physiol.* 84:157–186. doi:10.1085/jgp.84.2.157.

624 Yu, F.H., and W.A. Catterall. 2004. The VGL-Chanome: A Protein Superfamily Specialized for
625 Electrical Signaling and Ionic Homeostasis. *Sci. STKE*. 2004. doi:10.1126/stke.2532004re15.

626 Zhang, K., D. Julius, and Y. Cheng. 2021. Structural snapshots of TRPV1 reveal mechanism of
627 polymodal functionality. *Cell*. 184:5138-5150.e12. doi:10.1016/j.cell.2021.08.012.

628 Zubcevic, L., S. Le, H. Yang, and S.-Y. Lee. 2018. Conformational plasticity in the selectivity filter of
629 the TRPV2 ion channel. *Nat. Struct. Mol. Biol.* 25:405–415. doi:10.1038/s41594-018-0059-
630 z.

631

632

633
634
635 **Figure legends.**
636
637
638 **Figure 1. The voltage-dependence of TRPV1 is influenced by the permeant ion.**
639 **A)** Representative inside-out current-traces recorded in the same patch, elicited by 20
640 mV steps from -130 mV to 130 mV for a duration of 150 ms. The extracellular solution
641 (pipette) contained 130 mM NaCl, this patch was first exposed to internal 130 mM
642 NaCl (black) followed by exposure to 130 mM NaCl + 10 μM capsaicin (red) and finally
643 to 130 mM LiCl + 10 μM capsaicin (blue). All experiments were performed following
644 the same experimental strategy to compare the permeation of different monovalent
645 ions (Li^+, K^+, Rb^+, NH_4^+, Cs^+) with respect to the permeation of Na^+ in the same patch.
646 **B)** Averages of current-voltage (I-V) relations for all ions tested. The number of
647 experiments, n, is in parenthesis and is the same for panels C-E. **C)** Conductance-
648 voltage (G-V) relations for monovalent ions, obtained from data as in B in the presence

649 of 10 μM capsaicin, normalized to data with a symmetrical concentration of Na^+ from
650 each patch. G-V relations were fitted to equation 1 (continuous lines). **D)** Scatter plots
651 of the apparent charge z (above) and $V_{½}$ (below) associated with channel opening,
652 both were estimated by fitting G-V curves to equation 1. The values of z for Li^+ were
653 compared for statistical differences with all other ions, the p values are: *p = 0.00007
654 for Li^+ vs. Na^+; NS (not significant) p=0.213 for Li^+ vs. K^+; p = 0.00034 for Li^+ vs. Rb^+; p
655 = 0.00005 for Li^+ vs. NH_4^+; P = 0.01 for Li^+ vs. Cs^+. For $V_{½}$: p = 0.0000009 for Li^+ vs. Na^+;
656 p = 0.00001 for Li^+ vs. K^+; p = 0.00000001 for Li^+ vs. Rb^+; P = 0.000002 for Li^+ vs. NH_4^+;
657 p = 0.02 for Li^+ vs. Cs^+. **E)** Scatter plot of the $\Delta\Delta G$ associated to the ion effect in channel
658 opening was estimated as: $\Delta\Delta G = \Delta G_{Ion} - \Delta G_{Na^+}$. The * symbol indicates statistical
659 differences, p = 0.00005 for Li^+ vs. K^+; p = 0.0000002 for Li^+ vs. Rb^+; p = 0.000004 for
660 Li^+ vs. NH_4^+; p = 0.003 for Li^+ vs. Cs^+. Data are shown as mean ± SEM. The significant
661 difference was determined with a one-way ANOVA test followed by a Tukey´s test
662 post-hoc.
663
664 **Figure 2. TRPV1 permeability to monovalent ions is size-dependent.**
665 **A)** Representative current traces showing openings from single-channel recordings in
666 the presence of varying permeant ions. Inside-out patches were first exposed to
667 internal 130 mM Na^+ + 100 nM capsaicin and then to internal 130 mM (Li^+ (blue), Na^+
668 (red) K^+(mustard), Rb^+ (purple), NH_4^+ (black), Cs^+ (green)) + 100 nM capsaicin,
669 similarly to experiments in Figure 1A. The dashed line represents the closed state of
670 the channel. Currents are shown filtered at 2.5 kHz, for clarity of illustration. **B)** I-V
671 relations from single-channel records. These were obtained from data as in A for each
672 ion. **C)** Current carried by each ion relative to the single-channel current amplitude
673 with Na^+. All currents measured at 90 mV. Ionic radii in Å are also shown for
674 comparison. Data are mean ± s.e.m., n is shown in parentheses and is the same for the
675 curves in **B**.
676
677 **Figure 3. Rubidium ions strongly modulate the single-channel open probability**
678 **of TRPV1 channels.**
679 **A)** Representative current traces from single-channel recordings at 70 mV when
680 intracellular Rb^+ (purple) or Na^+ (red) were used as permeant ions. Currents are
681 shown at full bandwidth (5 kHz). **B)** Open probability of TRPV1 channels at 70 mV in
682 the presence of different permeant ions and 100 nM of capsaicin, calculated from
683 traces of current recordings as shown in A. Data are mean ± s.e.m. Number of
684 experiments is: Li^+(4); Na^+(8); K^+(3); Rb^+(5); NH_4^+(4); Cs^+(4).
685
686 **Figure 4. The permeant ion modulates single channel kinetics of TRPV1**
687 **channels. A)** Representative single-channel traces with the indicated permeant ion.
688 Data is shown at full bandwidth (5 kHz) except Li^+ currents, which are filtered at 2.5
689 kHz. **B)** Burst length distributions corresponding to permeant ions in A. The
690 continuous curve is the sum of exponential components. The values of time constants
691 (τ, in s) and amplitudes (a_i) are: Cs^+; a_1=1.5474, τ_1 = 0.0013, a_2=5.2727, τ_2=0.04818,
692 a_3=4.3972, τ_3=0.5031. Na^+; a_1=0.3720, τ_1=0.0362, a_2=3.2643, τ_2=0.8346. Li^+;

693 a_1=2.9447,τ_1=0.0048, a_2=8.0241,τ_2=0.2362. Rb^+; a_1=5.0377, τ_1=7.244 x 10^{-5},
694 a_2=8.7838,τ_2=0.0021, a_3=8.4035,τ_3=0.0163, a_4=2.8719, τ_4=0.2094.
695
696 **Figure 5. Fluctuations in the single-channel current during the open state can be**
697 **fitted by a Markov model.**
698 **A)** Representative current trace during a typical single TRPV1 opening burst recorded
699 in the inside-out configuration at 90 mV, with internal 130 mM RbCl + 100 nM
700 capsaicin. **B)** Normalized all-points histograms showing single-channel current
701 amplitudes of openings elicited by 100 nM capsaicin at 90 mV, for each ion tested. The
702 histograms are shown aligned to the closed state amplitude peak. **C)** All-points
703 histograms aligned to the maximum current amplitude of the open state to highlight
704 the asymmetric form of the histograms. **D)** The same histograms in C are shown
705 normalized both in number of counts and current amplitude. This representation
706 emphasizes the ion-dependence of the open current asymmetry. **E)** Current trace of a
707 single-channel at 90 mV from an inside-out patch exposed to internal 130 mM NH_4Cl +
708 100 nM capsaicin (black) and simulation with the model in Scheme I (blue). These
709 simulated recordings are used to produce simulated all-points amplitude histograms
710 of single-channel current, which are then fitted to experimental all-points amplitude
711 histograms. **F)** Typical fit of a simulated histogram (blue) to experimental histogram
712 elicited by 110 mV with internal 130 mM NH_4Cl + 100 nM capsaicin (black) using the
713 Markov model in Scheme I. Parameters obtained from the fit are: α_o = 1500 s^{-1}; α_c = 27
714 s^{-1}; β_o = 22500 s^{-1}; β_c = 600 s^{-1}; γ_o = 127500 s^{-1}; γ_c = 30000 s^{-1}; χ^2 = 0.00013873.
715
716 **Figure 6. Voltage-dependent transitions near the open state of TRPV1 channels**
717 **are modulated by the permeant ions.**
718 **A)** Rate constants obtained from the Markov model fit to the histograms as in Figure
719 5F. The rate constants were classified as slow, medium, and fast according to their
720 magnitude at 0 mV. The continuous curves represent the fit to Eq. 5.
721 **B)** Plot of the value of the rate constants at zero mV obtained from the fit of equation 5
722 to rate constants in A. Data are mean ± s.e.m. n is: 3 (Li^+); 6 (Na^+); 2(K^+); 3 (Rb^+); 3
723 (NH_4^+) and 3 (Cs^+).
724
725
726 **Figure 7. The opening probability predicted by the Markov partially model**
727 **explains the macroscopic experimental behavior.**
728 **A)** Representative inside-out macroscopic current traces recorded in the same patch,
729 elicited by 20 mV steps from -130 mV to +150 mV for 150 ms. The patch was exposed
730 to internal 130 mM NaCl + 10 μM capsaicin (red) followed by 130 mM RbCl + 10 μM
731 capsaicin (purple). **B)** Representative inside-out current traces like A but using 100
732 nM capsaicin. **C)** Normalized conductance-voltage (G-V) relations with monovalent
733 ions, obtained from inside-out patches after treatment with internal 100 nM capsaicin.
734 The G-V relation was fitted to the Boltzmann function (line). Data are shown as mean
735 ± s.e.m., number of experiments n, in parenthesis. **D)** Normalized prediction of open
736 probability by a Markov model for each monovalent ion. **E)** Bar graph of apparent
737 charge (q_{app})associated with channel opening estimated by fitting a Boltzmann
738 equation to curves in A and B. Data is shown as mean ± s.e.m.

Supplementary figure legends.

Supplementary Figure 1. Analysis of the open-closed kinetics of single-channel recordings in different permeant ions.
A) Open time distributions in the presence of the indicated ion. The blue curve is the fit of the histogram to a sum of exponential components. Each component is indicated by the curves in dotted lines. **B)** Closed time distribution in the presence of the indicated ion. The blue curve is the fit of the histogram to a sum of exponential components. Each component is indicated by the curves in dotted lines. The values of the time constants and amplitudes of exponential components are shown in Table 1.

Supplementary Figure 2. Gaussian fits to amplitude histograms of currents from different ions. The grey shaded and dotted curve is the best fit to each amplitude histogram to a single Gaussian function. Li^+ carried currents show the least extra open channel noise, as indicated by the extra counts between the Gaussian and the peak with zero current mean that indicates the closed channel level.

Supplementary Figure 3. Amplitude histogram fits to three different Markov models. A) Markov models with one closed state (green), two closed states (blue) and three closed states (red). **B)** Fit of the simulated histograms from the models in A to experimental an all-points histogram of single channel current of TRPV1(black), elicited by a pulse to 90 mV from an inside-out patches exposed to 130 mM NaCl + 100 nM capsaicin. The fits parameters used for one close state were: α_o = 301.9535 s^{-1}; α_c = 36.1664 s^{-1}; χ^2 = 0.0697; two closed states: α_o = 300 s^{-1}; α_c = 37.5 s^{-1}; γ_o = 28500 s^{-1}; γ_c = 13500 s^{-1}; χ^2 = 0.002342; three closed states: α_o = 280.61 s^{-1}; α_c = 49 s^{-1}; β_o = 14724.475 s^{-1}; β_c = 1133.16 s^{-1}; γ_o = 52500 s^{-1}; γ_c = 15396 s^{-1}; χ^2 = 0.00017296.

Appendix: Derivation of equation 6

The equations describing the occupancy of each state in Scheme I are given by

$$\frac{dC_s}{dt} = \alpha_c O - \alpha_o C_s$$

$$\frac{dC_m}{dt} = \beta_c O - \beta_o C_m$$

$$\frac{dC_f}{dt} = \gamma_c O - \gamma_o C_f$$

$$\frac{dO}{dt} = \alpha_o C_s + \beta_o C_m + \gamma_o C_f - O(\alpha_c + \beta_c + \gamma_c)$$

These equations are subject to: $C_s + C_m + C_f + O = 1$ and the probability of being in the open state, P_o is:

$$P_O = \frac{O}{C_s + C_m + C_f + O} = \frac{1}{1 + \frac{C_s}{O} + \frac{C_m}{O} + \frac{C_f}{O}}$$

In steady-state:

$$0=\begin{cases} \frac{dC_s}{dt} = \alpha_c O - \alpha_o C_s \\ \frac{dC_m}{dt} = \beta_c O - \beta_o C_m \\ \frac{dC_f}{dt} = \gamma_c O - \gamma_o C_f \\ \frac{dO}{dt} = \alpha_o C_s + \beta_o C_m + \gamma_o C_f - O(\alpha_c + \beta_c + \gamma_c) \end{cases}$$

Therefore: $\frac{C_s}{O} = \frac{\propto_c}{\propto_o}$; $\frac{C_m}{O} = \frac{\beta_c}{\beta_o}$; $\frac{C_f}{O} = \frac{\gamma_c}{\gamma_o}$ and $P_O = \frac{1}{1+\frac{\propto_c}{\propto_o}+\frac{\beta_c}{\beta_o}+\frac{\gamma_c}{\gamma_o}}$

$P_O = \frac{1}{1+\frac{\propto_c}{\propto_o}+\frac{\beta_c}{\beta_o}+\frac{\gamma_c}{\gamma_o}} \cdot \left(\frac{\frac{\alpha_o}{\alpha_c}}{\frac{\alpha_o}{\alpha_c}}\right) = \frac{\frac{\alpha_o}{\alpha_c}}{1+\frac{\alpha_o}{\alpha_c}+\frac{\alpha_o}{\alpha_c}.\frac{\beta_c}{\beta_o}+\frac{\alpha_o}{\alpha_c}.\frac{\gamma_c}{\gamma_o}}$. Defining $\frac{i_o}{i_c} = K_i \; for \; i = \propto, \beta \; or \; \gamma$, we can write:

$P_O = \frac{K_s}{1+K_s+\frac{K_s}{K_m}+\frac{K_s}{K_f}}$, where α=*s* stands for slow, β= *m* for medium and γ= *f* for fast.

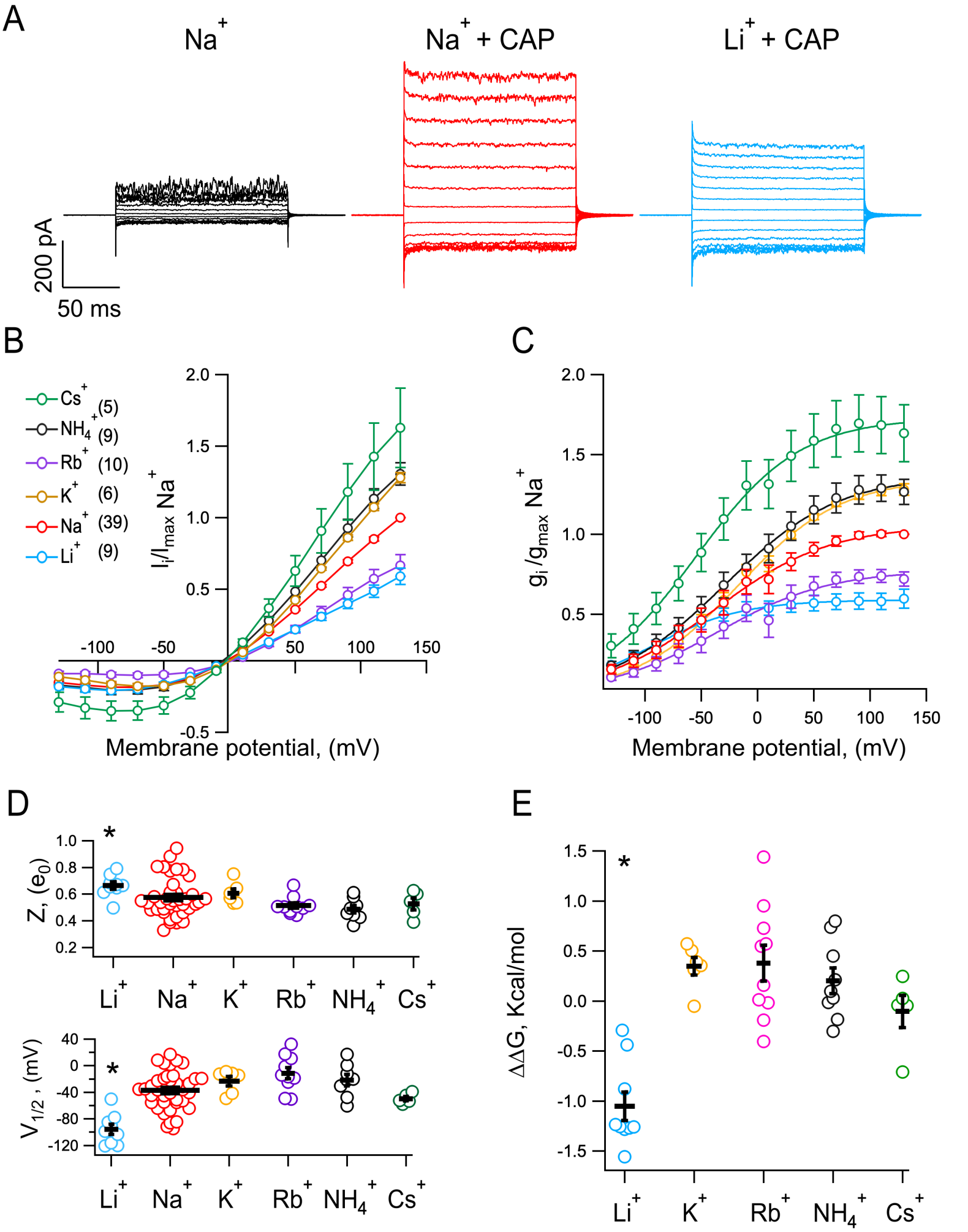
A
Na+
Na+ + CAP
Li+ + CAP
200 pA
50 ms
B
Cs+ (5)
NH4+ (9)
Rb+ (10)
K+ (6)
Na+ (39)
Li+ (9)
Ii/Imax Na+
Membrane potential, (mV)
C
gi /gmax Na+
Membrane potential, (mV)
D
Z, (e0)
V1/2 , (mV)
Li+ Na+ K+ Rb+ NH4+ Cs+
E
ΔΔG, Kcal/mol
Li+ K+ Rb+ NH4+ Cs+

Figure 1

A

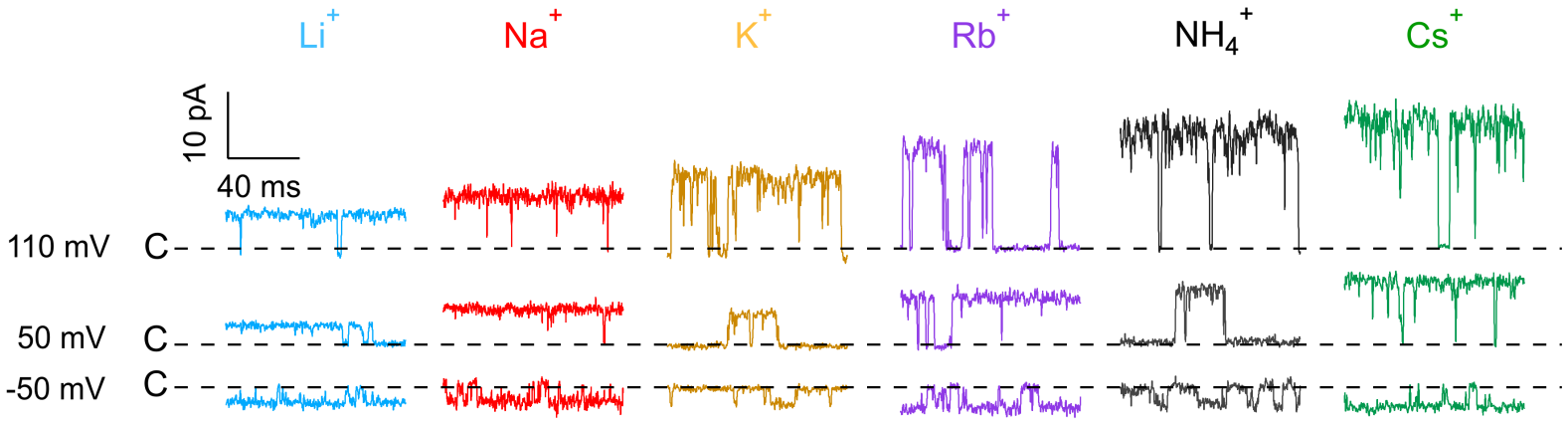

B

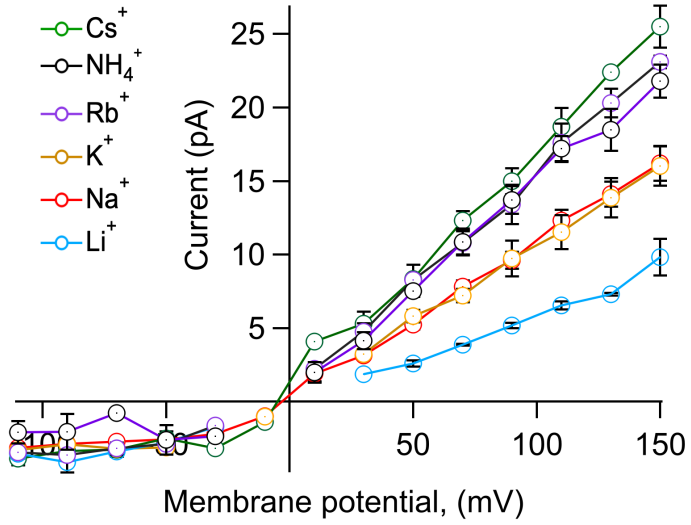

C

Ion	I_I/I_{Na^+}	Å
Cs^+	1.58 ± 0.15 (4)	1.69
NH_4^+	1.55 ± 0.19 (3)	1.48
Rb^+	1.28 ± 0.08 (5)	1.48
K^+	1.23 ± 0.20 (4)	1.33
Na^+	1	0.96
Li^+	0.48 ± 0.05 (4)	0.6

Figure 2

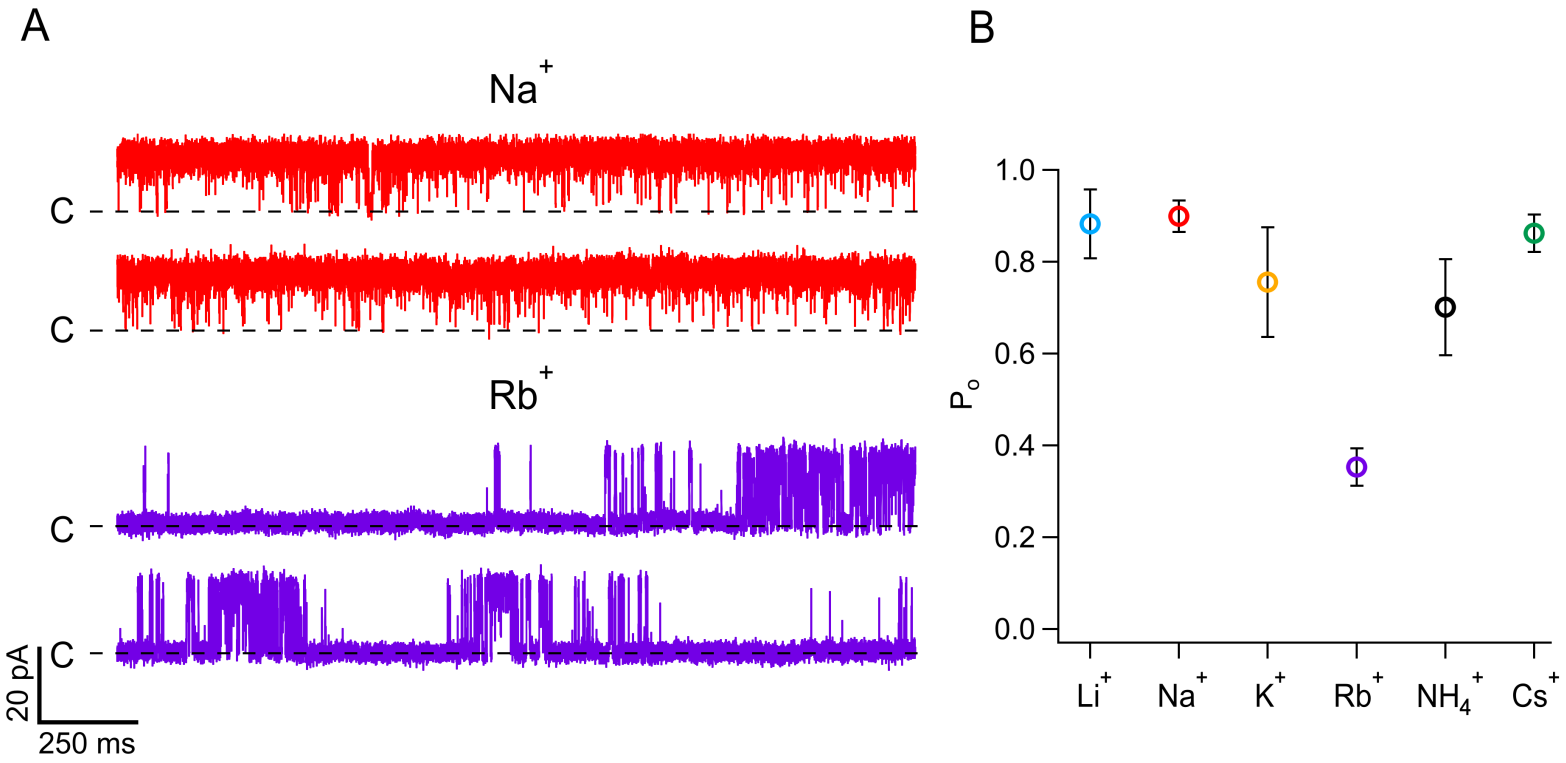

Figure 3

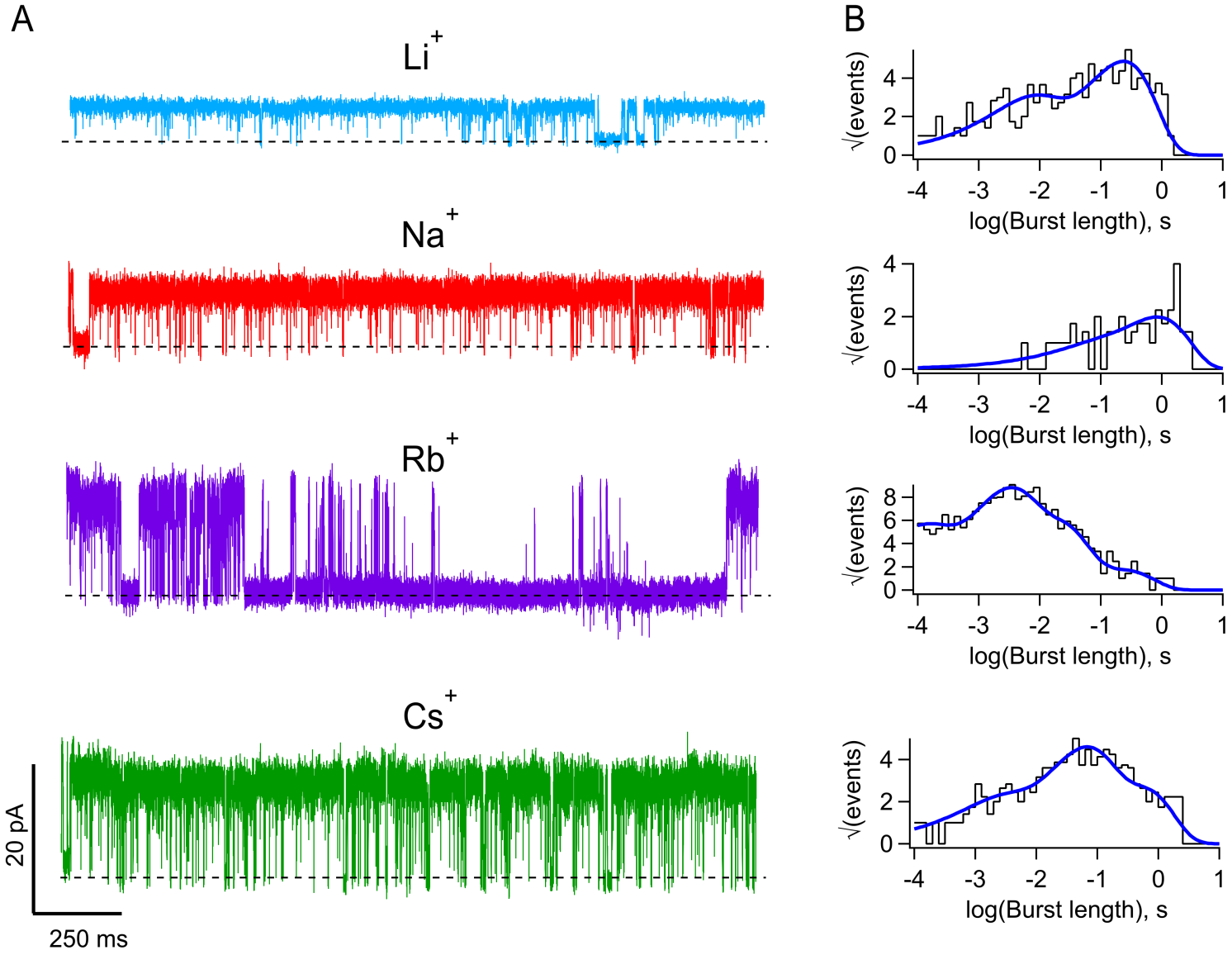

Figure 4

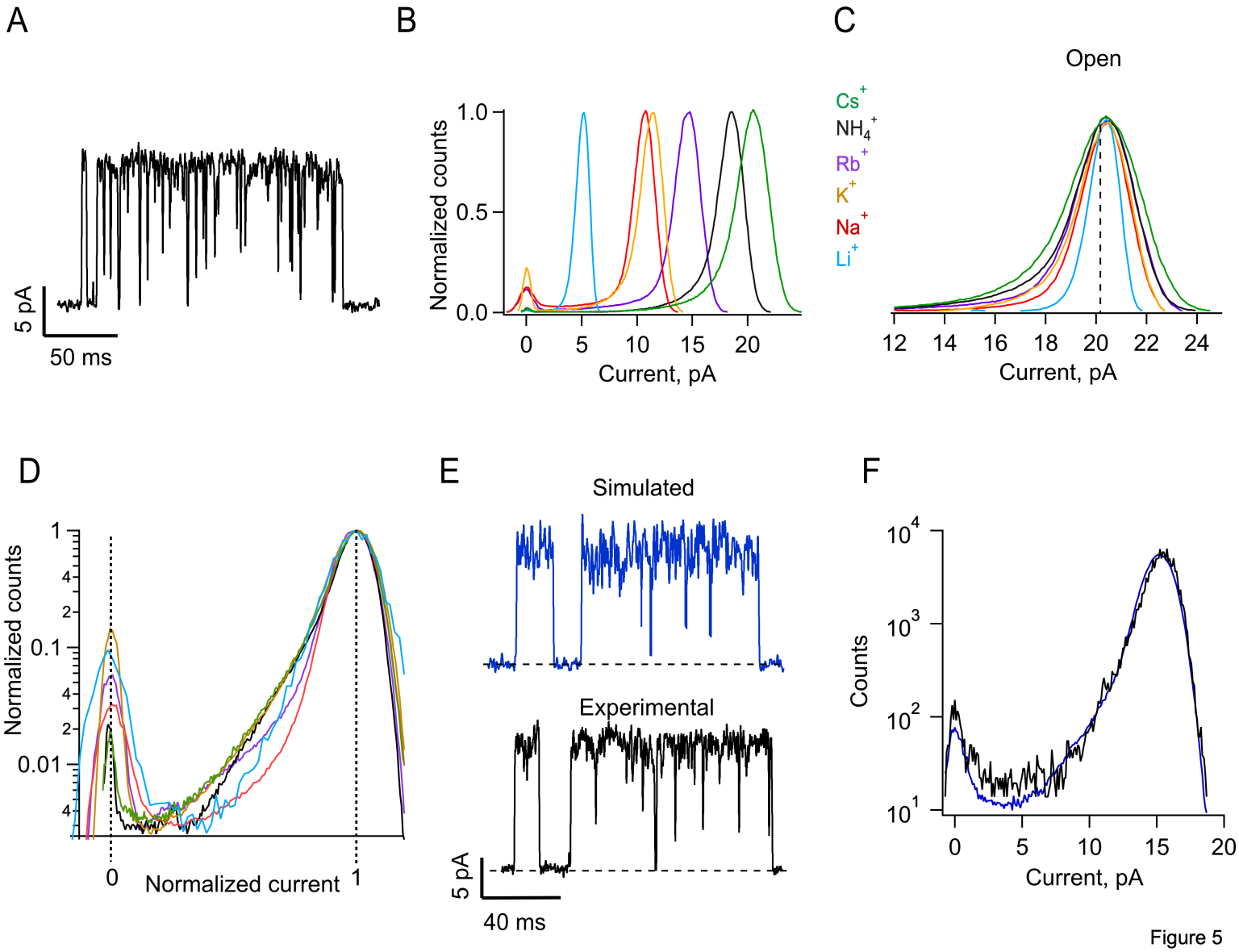
A
5 pA
50 ms
B
Normalized counts
1.0
0.5
0.0
0
5
10
15
20
Current, pA
C
Open
Cs+
NH4+
Rb+
K+
Na+
Li+
12
14
16
18
20
22
24
Current, pA
D
Normalized counts
1
4
2
0.1
4
2
0.01
4
0
Normalized current
1
E
Simulated
Experimental
5 pA
40 ms
F
Counts
10^4
10^3
10^2
10^1
0
5
10
15
20
Current, pA

Figure 5

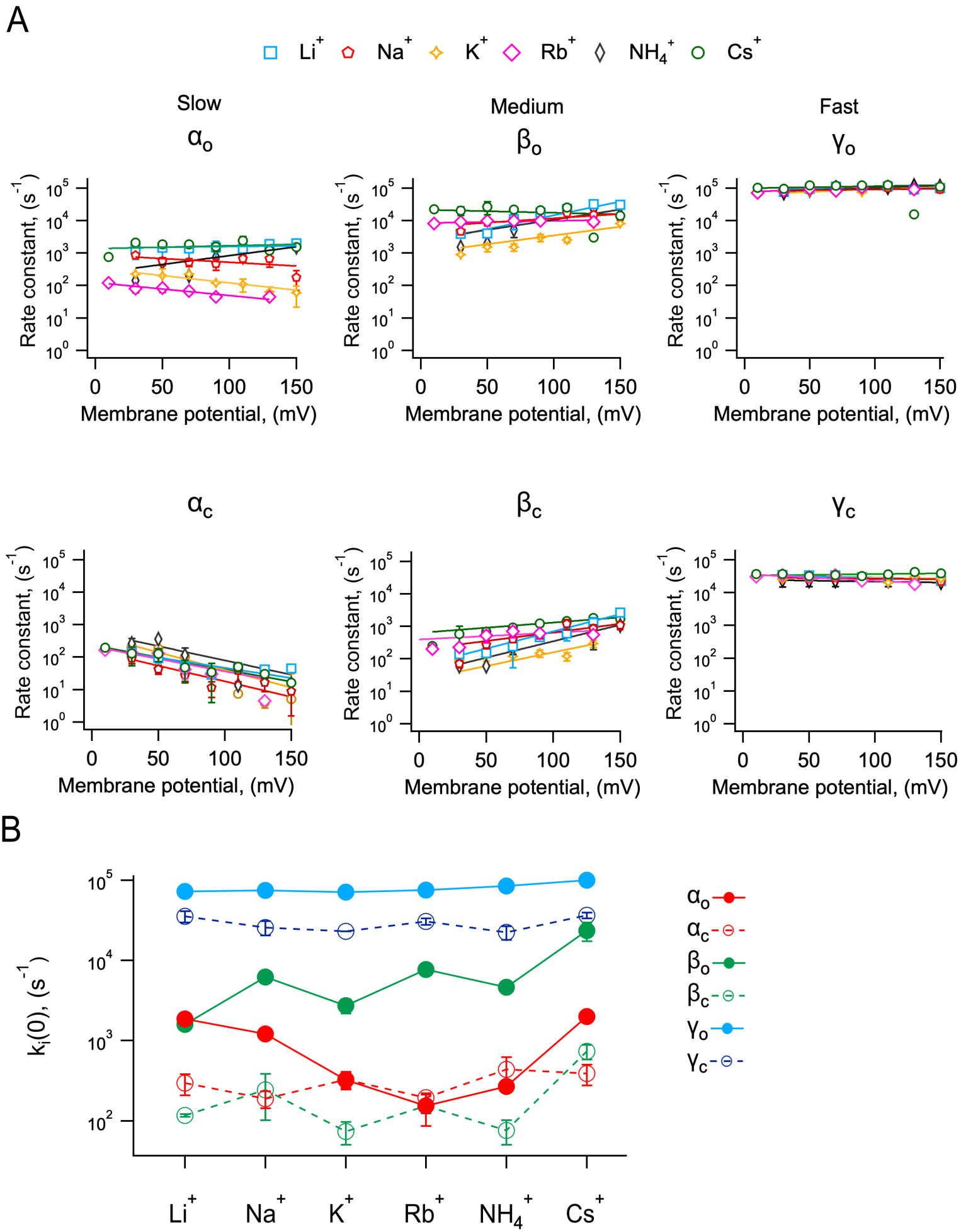
A
Li+ Na+ K+ Rb+ NH4+ Cs+
Slow
Medium
Fast
αo
βo
γo
αc
βc
γc
Rate constant, (s-1)
Membrane potential, (mV)
B
ki(0), (s-1)
αo
αc
βo
βc
γo
γc
Li+ Na+ K+ Rb+ NH4+ Cs+

Figure 6

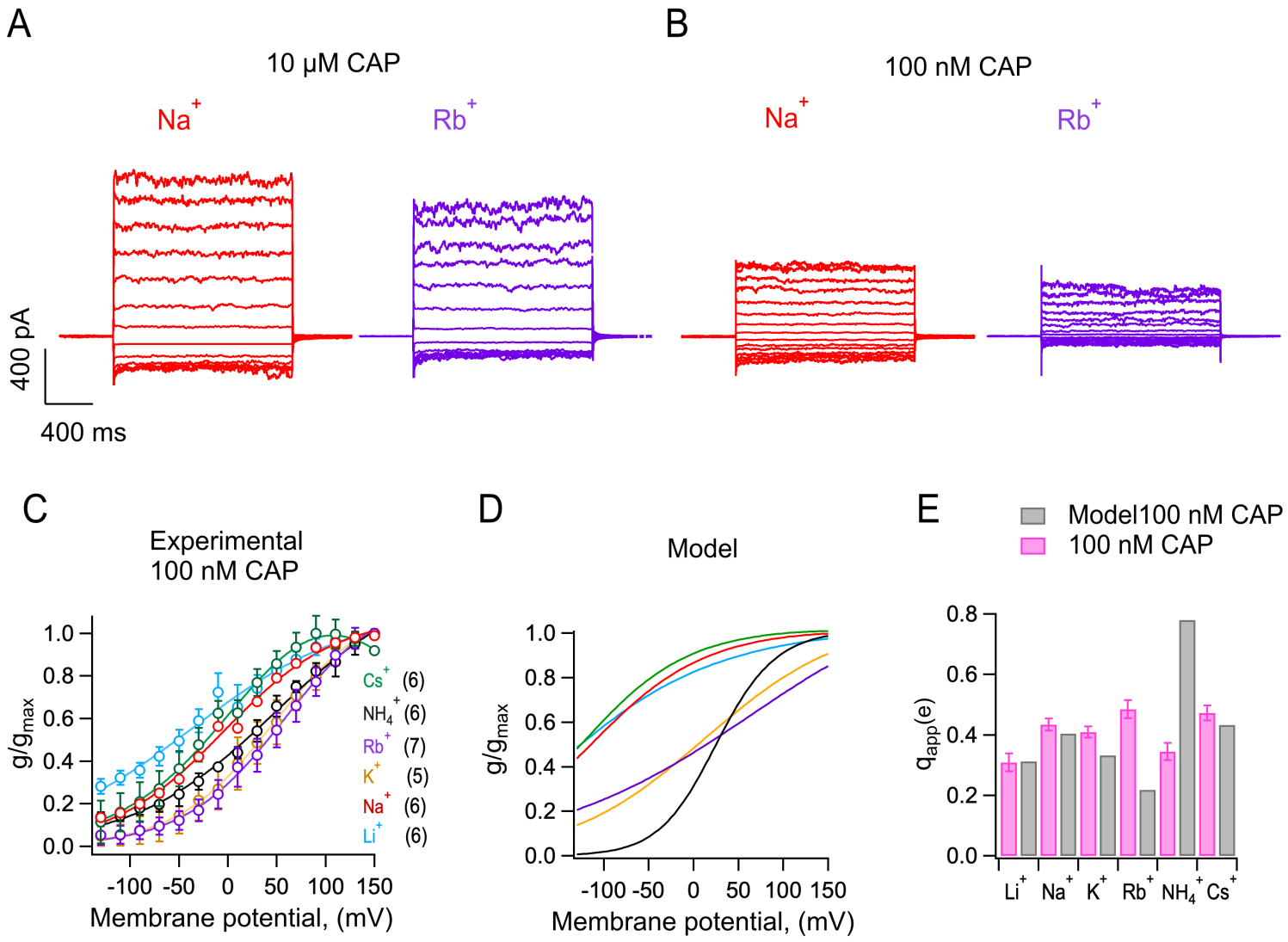
A
10 μM CAP
Na+
Rb+
400 pA
400 ms
B
100 nM CAP
Na+
Rb+
C
Experimental
100 nM CAP
g/gmax
Cs+ (6)
NH4+ (6)
Rb+ (7)
K+ (5)
Na+ (6)
Li+ (6)
Membrane potential, (mV)
D
Model
g/gmax
Membrane potential, (mV)
E
Model100 nM CAP
100 nM CAP
qapp(e)
Li+
Na+
K+
Rb+
NH4+
Cs+

Figure 7

Permeant ion	Open time		Closed time	
	Time constant (s)	**Amplitude**	**Time constant (s)**	**Amplitude**
Li^+	$\tau_1 = 0.0002$ $\tau_2 = 0.004$ $\tau_3 = 0.02$	$a_1 = 2.3$ $a_2 = 3.4$ $a_3 = 4.8$	$\tau_1 = 0.0001$ $\tau_2 = 0.0005$ $\tau_3 = 0.005$ $\tau_4 = 0.06$	$a_1 = 7.5$ $a_2 = 4.2$ $a_3 = 2.5$ $a_4 = 1.1$
Na^+	$\tau_1 = 0.0001$ $\tau_2 = 0.0015$ $\tau_3 = 0.011$	$a_1 = 11.6$ $a_2 = 2.3$ $a_3 = 16.6$	$\tau_1 = 6.7 \times 10^{-5}$ $\tau_2 = 0.0005$ $\tau_3 = 0.0033$ $\tau_4 = 0.0305$	$a_1 = 21.4$ $a_2 = 11.8$ $a_3 = 3.7$ $a_4 = 0.02$
Rb^+	$\tau_1 = 8.71 \times 10^{-5}$ $\tau_2 = 0.0011$ $\tau_3 = 0.003$	$a_1 = 13.1$ $a_2 = 12.5$ $a_3 = 21.5$	$\tau_1 = 6.6 \times 10^{-5}$ $\tau_2 = 0.0007$ $\tau_3 = 0.007$ $\tau_4 = 0.21$	$a_1 = 27.1$ $a_2 = 15.9$ $a_3 = 10.2$ $a_4 = 4.1$
Cs^+	$\tau_1 = 0.0001$ $\tau_2 = 0.0071$ $\tau_3 = 0.0211$	$a_1 = 16.5$ $a_2 = 25$ $a_3 = 5.6$	$\tau_1 = 8.5 \times 10^{-5}$ $\tau_2 = 0.0009$ $\tau_3 = 0.0038$ $\tau_4 = 0.023$	$a_1 = 31.5$ $a_2 = 15.5$ $a_3 = 6.2$ $a_4 = 2$

Table 1. Time constants and amplitudes of individual exponential components fitted to the histograms in supplementary figure 1.

Ion	Rate constants	Rate constant at 0 mV (s^{-1})	$Z_1(e_0)$
Li^+	α_o	1422.3	0.02548
	α_c	198.6	-0.36236
	β_o	2042.7	0.4883
	β_c	60.337	0.6112
	γ_o	87664.2	0.028629
	γ_c	34744	-0.051124
Na^+	α_o	875.09	-0.13178
	α_c	163.28	-0.55262
	β_o	6302.1	0.15402
	β_c	191.277	0.30446
	γ_o	83222	0.021433
	γ_c	28800.5	-0.02206
K^+	α_o	291.38	-0.20251
	α_c	357.04	-0.5549
	β_o	1000.6	0.312546
	β_c	22.5	0.4867
	γ_o	62298.3	0.10147
	γ_c	28322	-0.01003
Rb^+	α_o	123.32	-0.23134
	α_c	213.72	-0.44403
	β_o	8294.0	0.042546
	β_c	210.2	0.24134
	γ_o	78027.2	0.044316
	γ_c	36391	-0.11627
NH_4^+	α_o	236.23	0.31361
	α_c	596.9	-0.50654
	β_o	3077.9	0.32154
	β_c	33.656	0.582
	γ_o	72723.3	0.08284
	γ_c	24770.1	-0.034484
Cs^+	α_o	1543.1	0.014812
	α_c	231.63	-0.4304
	β_o	21545.9	-0.055021
	β_c	521.0	0.21361
	γ_o	97846	0.037125
	γ_c	34519	0.011

Table 2. Parameters of the fits to equation 5 of the data in Figure 6.

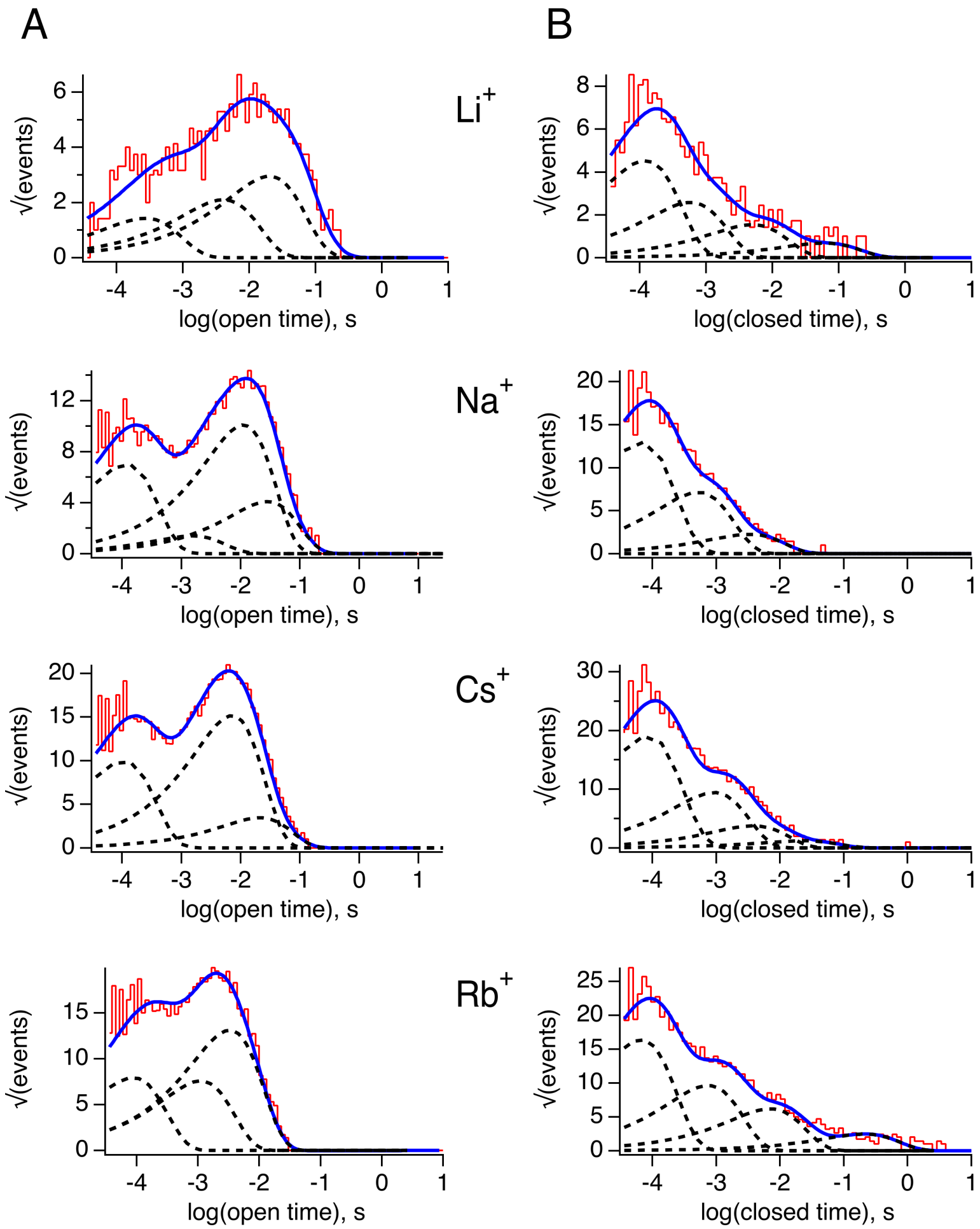

Supplementary figure 1

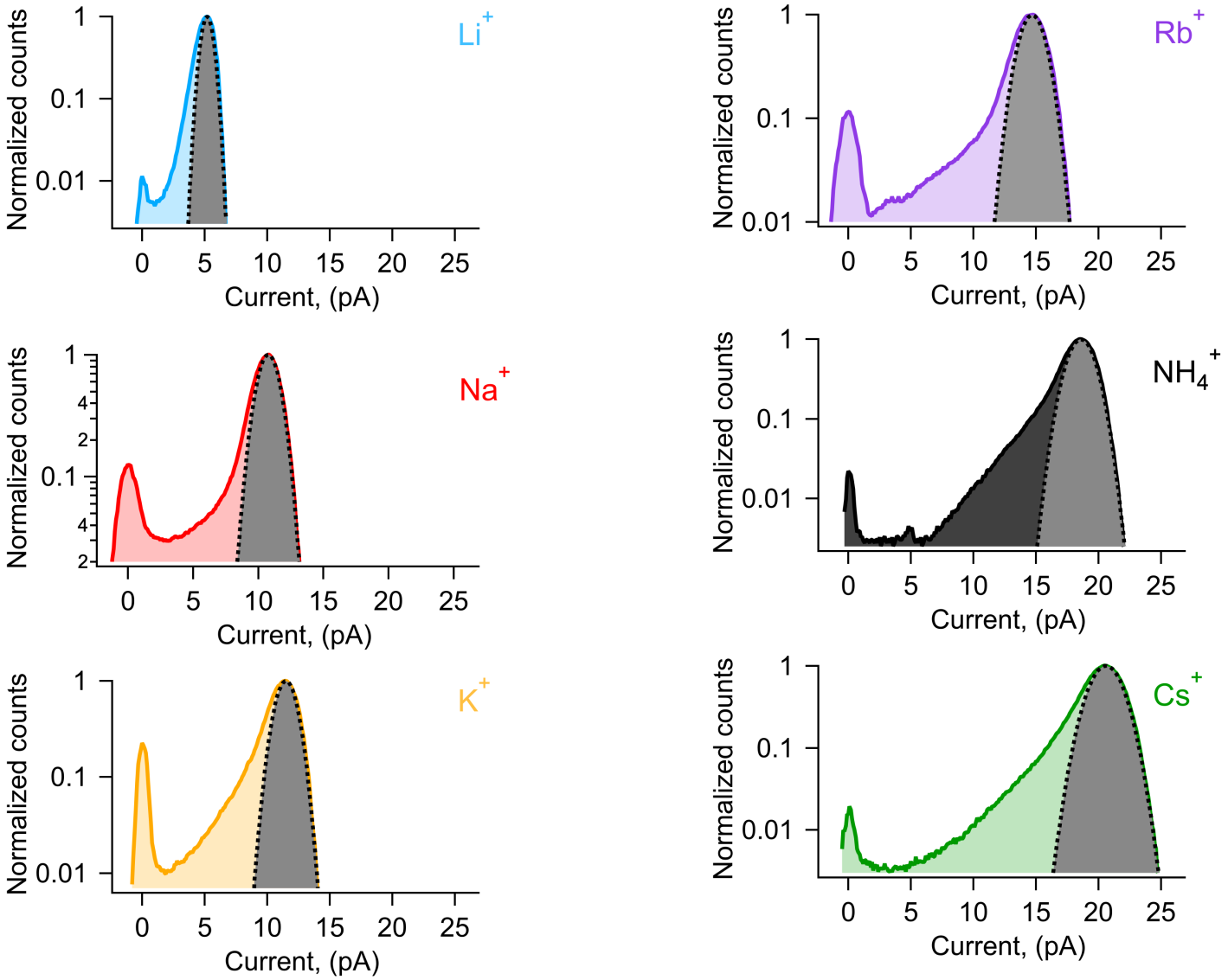

Supplementary Figure 2

A

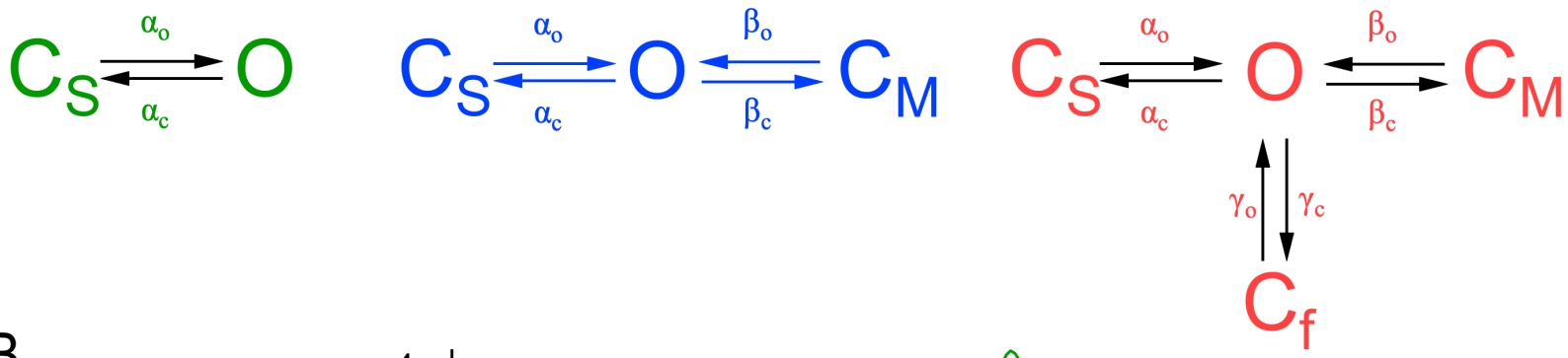

B

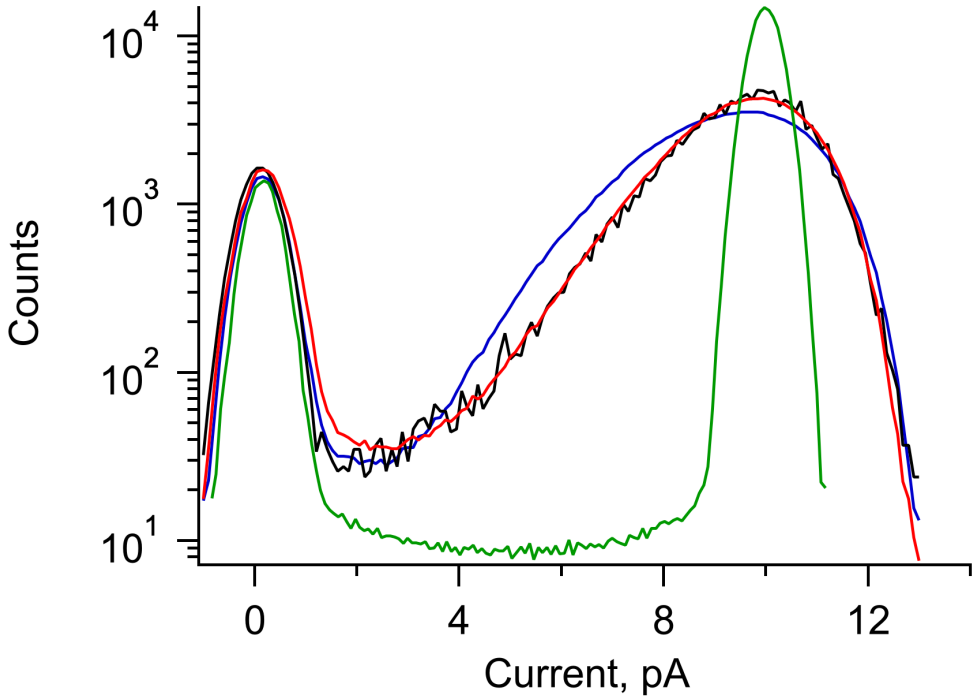

Supplementary figure 3